nature communications

Article

https://doi.org/10.1038/s41467-025-64991-x

Droplet impact on plasma surfaces: an interplay of the four states of matter

Received: 31 January 2025

Accepted: 30 September 2025

Published online: 14 November 2025

Check for updates

Jorge Ahumada Lazo & Yang Liu

Non-thermal plasmas such as dielectric barrier discharges (DBD) in the vicinity of liquids may induce water activation, interfacial deformation, and enhanced evaporation through charge, mass, and energy transport. Complexity increases when a solid surface is introduced into the system. Such multiphase interactions are central to plasma technologies in medicine, disinfection, wastewater treatment, and aerospace applications like flow control and de-icing. We experimentally investigated a water droplet impinging on the plasma-covered dielectric surface of a DBD actuator focusing on droplet dynamics, interfacial processes, and transient plasma response. This study reveals the complex interplay among four states of matter: solid, liquid, gas, and plasma. Key findings include enhanced droplet spreading, the formation of fingerlike structures, and the appearance of localized micro-discharges during droplet-plasma interaction. We also examine plasma discharge behavior, thermal processes during droplet spreading, breakup, and evaporation, and the disruption of ionic wind by droplet impact.

Plasma, defined as a partially or fully ionized gas, is widely regarded as the fourth state of matter[1]. While plasmas conform over 97% of the matter in the universe[2], they are not naturally abundant on Earth. Low-temperature plasmas can be artificially produced through high voltages, and can take the form of corona, direct current (DC) glow discharge, and dielectric barrier discharges (DBD). Within the DBD type, different regimes exist depending on the applied voltage waveform. Namely, these regimes are nanosecond pulse DBD, alternating current (AC) DBD (in the kHz regime), and radio-frequency DBD (in MHz). A second classification of DBD discharges is based on their electrode configuration. In general, a volume discharge occurs within the gap of two parallel plates, whereas a surface discharge takes place over a solid dielectric surface[1]. In its most basic form, a surface DBD actuator consists of a pair of asymmetrically positioned electrodes separated by a dielectric material. One electrode is enclosed by the dielectric material and the other one is exposed to air. When a high-voltage AC signal (in the order of 10 kV peak-to-peak and frequencies of 1–10 kHz) is applied between the two electrodes, a sheet of plasma develops along the edge of the exposed electrode and spreads for a few millimeters over the surface of the dielectric material. The electric field produced by the electrodes applies a body-force on the surrounding air that induces a stream in the gas phase (namely, the non-ionized air) over the actuator[3,4], this is known as ionic wind.

Due to the simplicity of actuators, fast response times, and the ease to manufacture complex actuator geometries, DBD plasmas have received considerable attention from the aerospace community for flow control purposes[3–6]. More recently, DBD actuators have been proposed for anti-/de-icing of airplane surfaces[7–9] by taking advantage of the thermal energy generated during the plasma discharge[10–13]. Outside of aerospace applications, plasma-based technologies have also been widely used in various fields, including plasma medicine, wastewater treatment, disinfection of drinking water, sterilization of medical equipment, surface treatment, and nanoparticle synthesis[14], among many other applications[15,16]. The fact that all of these applications involve the interaction of plasmas with another material (solid, liquid, or gas) is not coincidental. The versatility of plasmas for treating various materials relies on the highly reactive, non-equilibrium interfaces formed when plasma comes in contact with other substances[17]. During an atmospheric plasma discharge, reactive oxygen and nitrogen species (RONS) are formed along with excited molecules, ions, and UV photons[18]. This collection of highly reactive species and high-energy photons triggers a series of charge, mass, and energy transfer

Department of Mechanical Engineering, The City College of New York, New York, NY, USA. e-mail: yliu7@ccny.cuny.edu

processes that alter the chemistry and thus, the physical properties of substances.

In particular, plasmas generated within or in the vicinity of liquids give rise to a rich variety of phenomena such as water activation, surface deformation, droplet sputtering and enhanced evaporation resulting from the development of a dynamic plasma-liquid sheath which may modulate charge and heat exchange through the liquid's surface[19,20]. Despite being a relatively new field of study, the advancements in interface processes of plasma-liquid interactions have been indexed in several roadmaps (2012[21], 2016[16], and 2017[20]), reviews (2018)[22] and perspectives (2021)[19]. Plasmas can modify not only liquids but also solid surfaces[23–26]. For example, surface DBD plasmas can modify polymeric dielectrics by etching and deposition effects, which introduce irregularities to the surface, increasing its roughness, and thereby enhancing wettability[26]. A second mechanism is the so-called ion implantation through which some of the polymer's C-C and C-O bonds break, forming free radicals which can react with some of the RONS in the plasma, effectively introducing oxygen- and nitrogen-containing groups that increase the polarity at the surface[26].

It is important to note that, in addition to the various transport and reaction processes during the plasma-induced multiphase interactions, significant thermal effects are also present in DBD plasma. Despite the designation of cold plasma or non-thermal plasma, the temperature of the ionized gas molecules in a DBD discharge is higher than that of the non-ionized gas phase. Reported values of rotational and vibrational temperatures in AC-DBD plasmas during dry and wet actuation are presented in Table 1. Stanfield et al.[10] used emission spectroscopy to investigate the rotational and vibrational temperatures reached during DBD plasma actuation. Rotational temperatures were reported to vary from 465 K at the edge of the exposed electrode to 345 K at the end of the plasma discharge, whereas vibrational temperatures ranged from 3250 K to 2850 K at the same locations[10]. The heat generated by the collisions of ions and neutral molecules in the plasma is transferred by conduction to the solid materials in the actuator and by convection to the surrounding air.

While extensive work has been carried out to investigate the physics in DBD plasma for flow control, de-icing, and surface treatment, existing studies typically address either gas-phase plasma dynamics or quasi-steady liquid-plasma interactions in isolation. A comprehensive, time-resolved examination of droplet impact on plasma surfaces, in which charge transport, surface wettability alteration, thermal effects, and induced airflow evolve concurrently, remains lacking. In this work, we bridge this gap by employing high-speed imaging, Schlieren imaging, mist-seeding flow visualization, and infrared thermography to probe the thermal and dynamic behaviors of droplet impinging on a plasma-covered dielectric barrier surface. We thereby capture the rapid onset of enhanced spreading, finger-like instabilities driven by electrohydrodynamic forces, local micro-discharge phenomena at the triple-phase boundary, and the transient collapse of the plasma-induced ionic wind. These insights advance fundamental understanding of four-phase plasma–gas–liquid–solid interactions and inform the design of next-generation plasma-enabled technologies in aerospace, environmental, and biomedical applications.

In this study, we consider the case where plasma-liquid interactions take place on top of the dielectric material during surface DBD actuation following the impingement of a water droplet on the electrode-dielectric interface. This poses an intricate scenario that involves inertial, thermal, and electrical effects in which the four states of matter interact with one another. Some of the multiphase interactions, thermal processes, and phase change phenomena are conceptually illustrated in Fig. 1. It is to be noted from the schematic that every pair of phases have reciprocal effects. In the plasma-liquid relation, for instance, not only the liquid is affected by the plasma discharges as discussed above, but it has an effect on the plasma emissions. Namely, the combined electrical resistivity offered by the air and dielectric material increases due to the presence of the water droplet, thus disrupting the plasma emission and the overall performance of the actuator[27,28]. The impingement of droplet on solid surfaces has been extensively studied in the past two centuries[29–31]. Various impinging outcomes have been characterized, such as spreading, bouncing, and breakup dynamics, which are generally governed by Reynolds and Weber numbers. The presence of plasma during droplet impingement on a solid surface, however, introduces significant complexities. Some of the observed interactions in this study are illustrated schematically in Fig. 2, where the entire process from droplet impact to its complete evaporation is depicted. Namely, plasma alters the wettability properties of the dielectric surface[32–34]. Further, as the water is activated from contact with the plasma, its surface tension decreases. This affects the spreading of the droplet onto the surface. The droplet in contact with the actuator increases the electrical resistivity and disrupts the emission of plasma. For this study, individual droplets ($d \sim 2.75$ mm) of distilled water with electrical conductivity of 8 − 9 μS/cm were released from a height of 40 cm above the surface of an active DBD actuator. The dielectric material on which the droplet impacts and spreads is made out of polymethyl methacrylate (PMMA) covered with black enamel paint. Reported values of thermal conductivity of PMMA range between $k = 0.1922 - 0.1986$ W/(m · K) for a temperature range between 308 to 353 K[35].

The needle dispensing the water and the actuator were aligned so that the droplet impacted on the edge of the exposed electrode, covering the width of the plasma discharge while the droplet spread. Thermal infrared and high-speed imagery were used to characterize the thermal and dynamic processes that occurred over time scales ranging from 10 ms to 100 s and the interactions among the droplet, the plasma, the dielectric surface, and the induced airflow over the various time scales. Here, we describe these multi-phase interactions with a particular focus on: (1) the effect of the plasma on droplet spreading, (2) the role of the droplet as a liquid electrode during plasma actuation, (3) the transient dynamics of the induced airflow, and (4) the heat transfer mechanisms that lead to droplet heating and evaporation.

Table 1 | Reported values of rotational and vibrational temperatures in AC-DBD plasmas during dry and wet actuation

Type of plasma discharge	T_{rot} (K)	T_{vib} (K)	Authors
Surface AC-DBD, dry actuation	345 − 465[†]	2850 − 3250[†]	S.A. Stanfield et al.[10]
Surface AC-DBD, dry actuation	380 − 420[‡]	3000	B. Dong et al.[11]
Filamentary AC-DBD, dry actuation	650 − 850[*]	4.0 ± 2.0	N. Jidenko et al.[58]
Single filament AC-DBD to one water electrode	750 ± 150[¶]	4200 ± 500	P. Vanraes et al.[44]
AC-DBD between two water electrodes	520 − 680[§]	2600 − 2800[§]	L. Dong et al.[42]

[†]Variation in location within the discharge.
[‡]Variation in frequency 1 − 2 kHz.
[*]Variation in input power 15 − 35 W.
[¶]With electrode gap of 1.0 mm and voltage amplitude of 6.7 − 8.5 kV.
[§] Variation in electrode gap 0.1 − 0.3 mm and voltage amplitude 4.8 − 6.2 kV.

https://doi.org/10.1038/s41467-025-64991-x

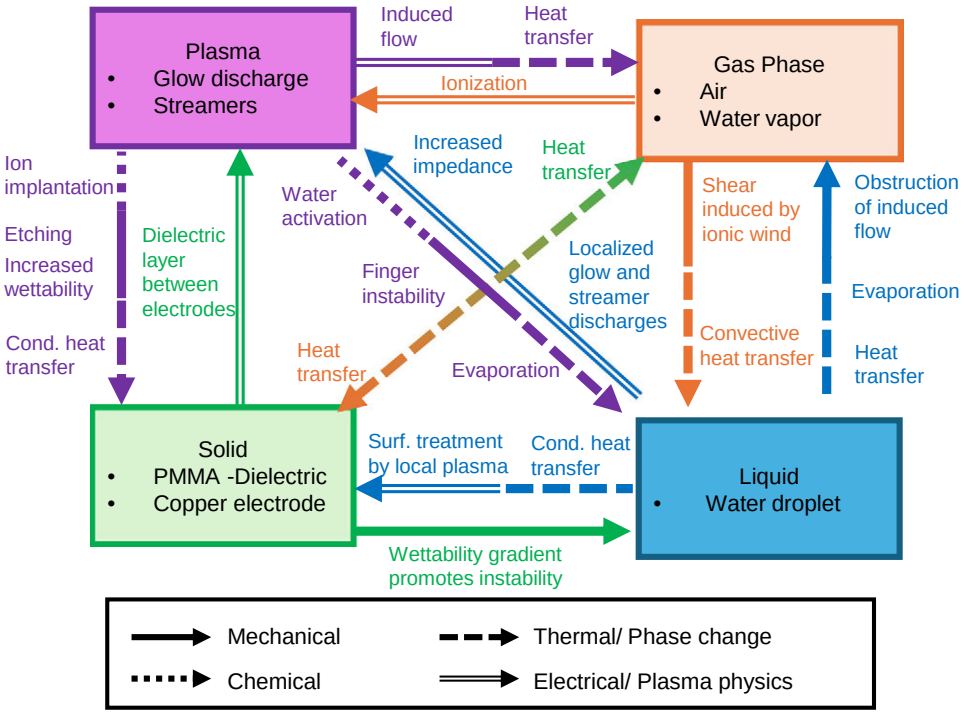

Fig. 1 | Conceptual map of the multiphase interactions. Schematic of some of the interfacial exchanges and processes taking place during water droplet impact on a plasma-covered surface.

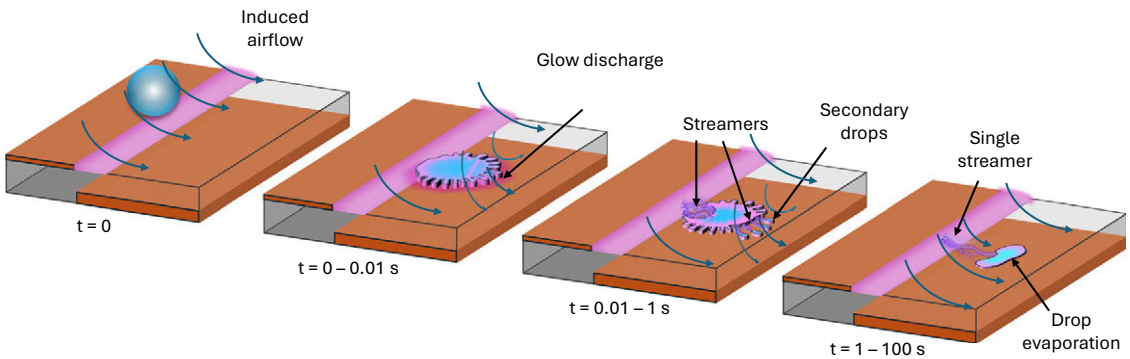

Fig. 2 | Temporal evolution of water droplet impacting a DBD actuator. The droplet spreads over the dielectric surface within 10 ms forming finger-like structures from which tips glow plasma is emitted radially outward. After ≈ 0.5 s, some of the finger-like structures separate from the bulk of the droplet due to evaporation. Simultaneously, the droplet separates from the exposed electrode. Multiple high-energy streamer discharges form between the electrode and the primary droplet and between the primary and secondary droplets. Within 30 s, all finger-like structures and secondary droplets evaporate, and a single streamer remains at the back of the droplet.

Figure 2 schematically illustrates the sequence of processes that take place over the various time scales. The first frame in Fig. 2 shows the instant prior to droplet impact ($t = 0$). The picture reveals the sheet of plasma formed along the edge of the exposed electrode (left) and propagating over the dielectric surface toward the encapsulated electrode (right). At $t < 0$, a steady stream of air flow is established by the plasma discharge. The airflow originates from the region above the exposed electrode and flows parallel to the plasma over the dielectric. Upon impact, within 10 ms the droplet spreads into a crown shape resulting from a fingering instability. Since the film of liquid maintains contact with the exposed electrode, charges accumulate at its surface, and the water acts as a liquid electrode. This results in the emission of plasma from the tips of the finger-like structures which modifies both the location and the direction of the induced airflow since it now takes place at the front edge of the droplet and is directed radially outward.

Within one second, the liquid begins to evaporate due to the combined effect of ohmic heating and high temperatures on the dielectric surface which is in turn heated up by the frequent collisions of ions and molecules in the plasma. Evaporation is favored near the exposed electrode, where the plasma intensity is highest, and at the base of the finger structures. This results in the formation of secondary droplets (formerly the finger tips) as well as the separation of the primary droplet from the electrode, shown in the third frame of Fig. 2. High-intensity filaments of plasma (or streamer discharges) appear in regions where the water has evaporated. The streamers produce local areas of high temperature which promote circulation within the liquid and evaporation of the droplet. Once the secondary droplets have completely evaporated and the remaining liquid has separated from the exposed electrode, a single streamer is observed (fourth frame in Fig. 2). This streamer connects the exposed electrode to the liquid film

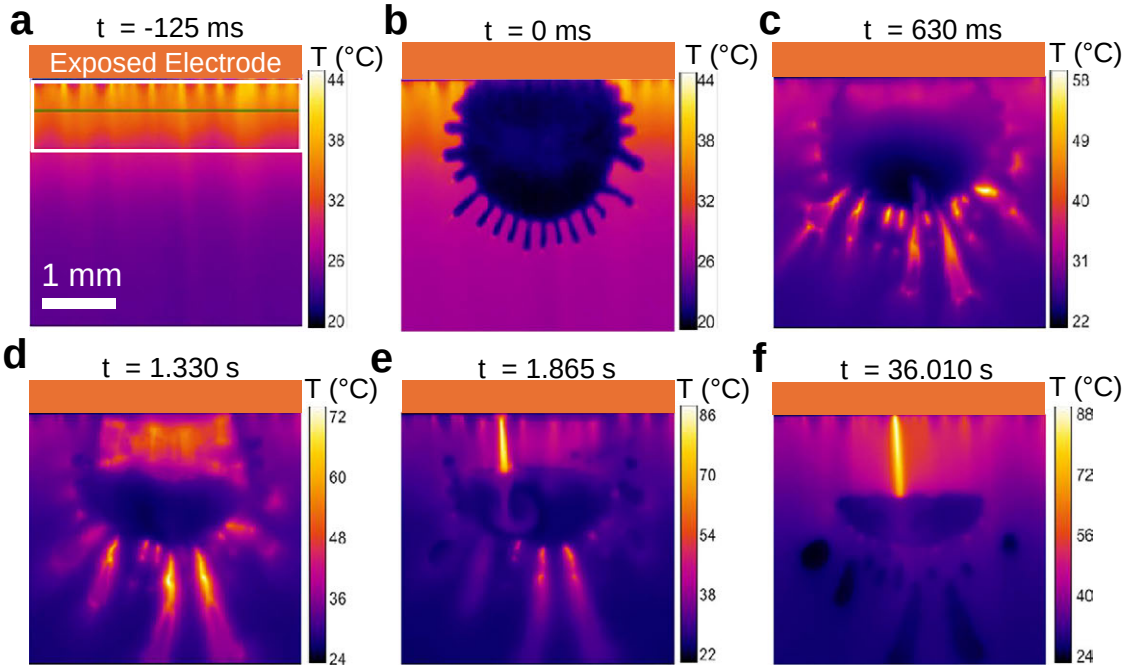

Fig. 3 | Thermal processes in the liquid-plasma-solid interactions. a–f Infrared thermal imagery of the actuator during droplet impact reveal the formation of fingers during the spreading phase, followed by glow and streamer plasma discharges around the liquid.

and drives its evaporation. The following sections address the thermal and dynamic mechanisms underlying the aforementioned observations as well as the phase changes and phase interactions that take place at each stage.

Results

Effect of plasma on the surface properties

It has been established that non-thermal plasmas can alter the surface roughness and composition of polymers, effectively increasing their wettability[23–26]. This is demonstrated in Fig. S1 in the Supplementary Material, where measurements of the contact angle (CA) between a water droplet and (a) an untreated actuator surface (static CA), (b) a plasma-treated surface (static CA), and (c) during plasma actuation (advancing CA). High-speed images of the back-illuminated droplet were taken at 500 fps with an exposure time of 1/10,000 s. Measurements of CA were carried out using third-degree polynomial fitting to the edge of the droplet using MATLAB. A water droplet was placed at the interface of the exposed electrode and the painted PMMA surface of the actuator. The droplet then rests over the two materials allowing for the measurement of both static contact angles. During the contact angle measurements as well as the following experiments, the ambient temperatures and relative humidity were maintained at $T_{amb} = 20$ °C and RH = 40%. At the untreated actuator interface, the droplet has a static CA of 56.3° on the copper electrode surface and 69.1° on the painted PMMA surface, as marked in Fig. S1 (a) in blue and red, respectively. The surface was then treated with a continuous plasma discharge ($V_{pp} = 23.8$ kV) for a duration of one minute. A second water droplet was placed at the interface and quickly displaced toward the dielectric such that its leftmost point barely touched the electrode-dielectric interface, as shown in Fig. S1 (b). After plasma actuation, the CA at the electrode and dielectric decreased to 36.6° and 25.7°, respectively.

The third test was conducted by applying a low intensity plasma ($V_{pp} = 14.2$ kV) to the droplet sitting on the actuator after test 2. With the plasma discharge, the droplet further displaced away from the electrode, with an advancing contact angle of 14.8°. During this process, the contact angle at the end of droplet contacting the edge of the electrode decreased to 30.9°. It should be noted that after certain time of actuation, the droplet entirely detaches from the electrode. This is followed by the formation of filamentary plasma structures between the electrode and the droplet. At this stage, measurement of contact angle is difficult due to the rapid changes in light intensity and droplet shape. Higher plasma intensities lead to a faster separation of the droplet, hence a low plasma intensity was used for this test to ensure sufficient time for image acquisition. Our results which indicate a decrease in CA due to plasma treatment are consistent with those reported in the literature[25,26,36].

Thermal processes

The dynamic phenomena presented in Fig. 2 hold a close relationship with the thermal processes taking place among the four phases. Heat is generated by the frequent collisions of electrons, ions, and neutral molecules in the plasma[10–13], and is then dissipated to the solid surfaces (electrodes and dielectric) through conduction, and to the gas phase by forced convection under the action of the induced flow. As outlined by Liu et al.[7], as a water droplet moves through the hot air in the plasma region, it is heated up by forced convection. Upon impact, heat is transferred from the hot dielectric surface by conduction. Thus, it is evident that the thermal properties of the solid and gas phases play a key role in the heat transfer within the system. In sessile droplets evaporating in the diffusion-controlled regime (i.e., in the absence of plasma), evaporation flux is greater at the contact line[37,38]. The overall evaporation rate is greatly influenced by the thermal conductivity, k, of the substrate[39–41]. In our experiments, the droplets spread over the interface of two materials with contrasting conductivities: the copper electrode with $k = 400$ W/(m · K) and PMMA dielectric of $k \approx 0.20$ W/(m · K)[35]. The contact area is modulated by the surface wettability, which was addressed in the previous section, where a significant decrease in contact angle resulted from plasma treatment of the surface and from active emissions. A second mechanism that contributes to droplet evaporation is the ohmic heating caused by the current flow through the liquid phase. These processes are discussed below for the various stages of the multiphase interactions.

https://doi.org/10.1038/s41467-025-64991-x

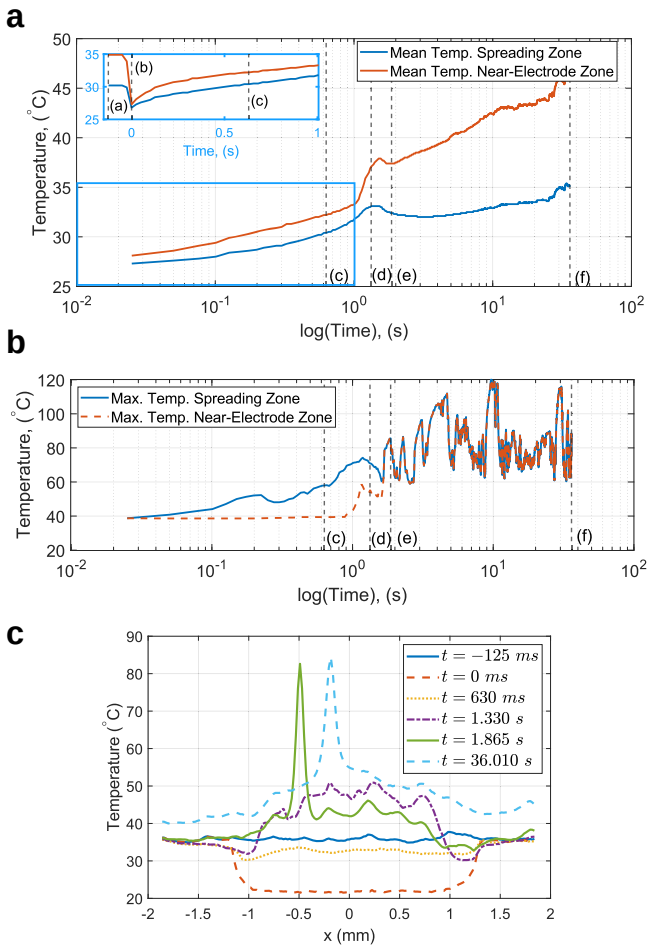

Fig. 4 | Surface temperatures during droplet-actuator interaction. a Temporal evolution of the mean temperature of the frames (**a**–**f**) in Fig. 3 and the near-electrode zone marked by the white rectangle in (**a**).**b** Temporal evolution of the maximum temperature and the near-electrode zone marked by the white rectangle in Fig. 3 (**a**). **c** Temperature profile near the electrode along the green line marked in Fig. 3 (**a**), at the instants in frames (**a**–f).

When the water droplet impacts the actuator, a series of thermal processes occur between the plasma-actuator system and the liquid. The infrared images acquired at 200 fps and having an exposure time of 1/200 s in Fig. 3a–f reveal the thermal effects of plasma emissions on the dielectric surface as well as the transient morphology of the droplet. Figure 4a shows the temporal evolutions of the mean temperature in the droplet spreading region included in Fig. 3a–f during the entire process of droplet impact and evaporation, as well as the mean temperature of the 1 mm thick zone of plasma near the electrode (indicated in the white rectangle in Fig. 3a). The inset in Fig. 4a shows the temperature evolution within the first second of droplet impact in linear time scale. Figure 4b shows the temporal evolution of the maximum temperatures in the same two regions. The dashed vertical lines in Fig. 4a, b indicate the times (> 0) of Fig. 3a–f. The temperature profiles through the centerline of the near-electrode zone (marked in green in Fig. 3a) are plotted in Fig. 4c. The Supplementary Video 1 accompanying this paper simultaneously presents the aforementioned thermal observations with high-speed imagery of the same event.

Before droplet impact ($t < 0$) in Fig. 3a, the temperature distribution of the dielectric material is presented. Two features of interest are the presence of hot spots localized along the edge of the exposed electrode and the temperature gradient along the streamwise direction (i.e., perpendicular to the electrode edge). The temperature is highest just next to the electrode ~ 40 °C for the case presented (see also the temporal plot of maximum temperature in Fig. 4b). The surface temperature decreases with increasing distance from the electrode edge (to ~ 23 °C), positively correlating with the perceived plasma intensity.

As the droplet impacts and spreads (Fig. 3b, t = 0 ms), it quenches the surface momentarily. Note the temperature of the surface of the droplet is 20 – 22 °C, while the temperature of the surroundings preserves the streamwise gradient described above. The rapid cooling of the surface at droplet impact can be seen in the inset of the plot in Fig. 4a at $t = 0$, as well as by comparing the temperature profiles in Fig. 4c for $t = -125$ ms and $t = 0$. The fully-spread droplet exhibits the finger-like structures mentioned above. The spreading and finger formation will be addressed in a later section. Although the temperature of the liquid is cooler than the surrounding surface, there exists a temperature gradient within the droplet normal to the edge of the electrode (the front edge of the droplet has a darker tone than its base touching the electrode). The thermal image in Fig. 3b reveals a faint emission of plasma originating from the tips of the finger-like structures, seen as bright specks protruding outward from the fingers. Figure 5b and Supplementary Video 2 illustrate the fingertip emissions more clearly. These glow emissions, however, have little thermal effect compared to the glow emission from the electrode.

After spreading, the droplet is disproportionately heated by conduction from the solid surface due to the pre-existing temperature gradient in the dielectric. This causes a higher temperature at the droplet's base, as seen in Fig. 3c. It is noted that the temperature at the base of the droplet is similar to that of the zone of plasma emission immediately adjacent to the electrode outside of the droplet (~ 35 °C). This is reflected by the low variance in the temperature profile shown in Fig. 4c for $t = 630$ ms. The period of droplet heating is reflected in Fig. 4a where the mean temperatures increase fairly steadily for $t <\sim 1$ s.

Besides the droplet's base, the thin fingers heat up more rapidly than the bulk of the droplet. These hot zones (base of the droplet and fingers) have a two-fold effect: first, surface tension is decreased due to the high temperatures, setting up thermal Marangoni flows; and second, evaporation is enhanced. The two effects reinforce each other, leading to a rapid thinning of the liquid film, which in turn results in a faster heating. This process causes the eventual separation of the fingers, forming secondary droplets (shown in Fig. 3c), as well as the separation of the droplet from the electrode edge (illustrated in Fig. 3d). It is important to differentiate between the previously mentioned fingertip emissions and the secondary streamers. The former are glow-like emissions coming out of the finger structures prior to secondary droplet separation. On the other hand, the secondary streamers are filamentary plasma structures formed between primary and secondary droplets during separation. The bright streaks around the droplet in Fig. 3c indicate the formation of secondary streamers during finger separation. These streamers are herein referred to as "secondary streamers" due to their relationship to the newly formed secondary droplets. The high-temperature streamers "inject" heat to the bulk of the droplet, which is dissipated by convection. This can be seen at the center of Fig. 3c, near the far-end droplet edge, as two of the bright streamers leave behind a thermal footprint that penetrates into the liquid. The Supplementary Video 1 elucidates the convective behavior of the thermal plume into the droplet, not appreciable by the still image in Fig. 3c. It is worth pointing out that the highest temperatures achieved during this period are those resulting from the secondary streamers at the fingers. The plot of maximum temperatures in Fig. 4b indicates that the near-electrode zone maintains a constant value of 40 °C while the radial streamers elsewhere in the spreading region reach temperatures of 50 – 70 °C.

Separation from the electrode occurs in three stages: first the droplet splits near its base in such a way that a small portion of the liquid remains in contact with the electrode. At this point (Fig. 3d), multiple high-intensity streamers bridge the two separated puddles of

liquid. This effect is reminiscent of the work of Dong et al.[42]. between two liquid electrodes. These are referred to as "primary streamers" and rapidly appear and disappear at various locations simultaneously. Using high-speed imagery at 20,000 fps, up to five streamers have been seen to form within a single AC cycle. These high-intensity streamers introduce heat at the base of the primary droplet. Due to the rapid fluctuation of streamers, the heating appears almost homogeneous along the base line, see for instance the temperature profile in Fig. 4c for $t = 1.330$ s. Besides heat, the streamers also impart momentum to the droplet which combined with the thermal Marangoni flow promote the migration of both the primary and secondary droplets further downstream. It is pointed out that several of the secondary droplets in Fig. 3d exhibit a stronger streamer discharge (with respect to Fig. 3c, as suggested by the plot of maximum temperature in Fig. 4b), reaching temperatures ~70 °C. Simultaneously, these secondary droplets are propelled further apart from the primary droplet, i.e., toward the bottom of Fig. 3d. As the secondary droplets migrate away from the primary one, the strong secondary streamers fade and the primary streamers become dominant, as suggested by the merging of the two curves in Fig. 4b. This indicates that the maximum temperatures in the spreading zone are now included in the near-electrode region. The second stage of separation occurs as the gap between the two liquid puddles widens due to evaporation, and the number of streamers decreases until only one is visible, as shown in Fig. 3e. While liquid is covering the electrode, the streamer has rather high mobility along the extent of the droplet. The third stage begins when the liquid contacting the electrode evaporates and the streamer is then established between the solid electrode and the liquid as shown in Fig. 3f. At this stage, the streamer is much less movable, appearing repeatedly at the same location. In addition, a "memory effect" is seen in which the streamer may shift between a few different locations, constantly returning to one of the previous spots. It is worth pointing out that high-speed imagery at 20,000 fps revealed the formation of only one streamer per AC cycle during the second and third stages, contrasting with up to five streamers forming simultaneously during the first stage of separation. In the two later stages, the single streamer has a very distinct temperature spike profile with respect to its surroundings, reaching temperatures over 100 °C, as indicated by the spikes in Fig. 4b.

The streamers impart heat and momentum to the droplet as they impact on the droplet's surface. A mushroom shaped thermal structure can be seen inside of the droplet in Fig. 3e. The structure forms at the hot spot where the streamer touches the liquid. It then propagates within the droplet through advection from the imparted momentum, establishing a forced convection inside of the droplet. The liquid continues to heat up and evaporate (Fig. 3f) under the action of the single streamer which remains nearly steady. A secondary effect of the high-temperature streamer is the heating of the surrounding dielectric surface. The temperature profiles in Fig. 4c show the heating up of the zones around the peak.

It was posited at the beginning of this section that in the absence of droplet impact, the induced airflow or ionic wind played a role in dissipating heat by forced convection. As discussed in-depth in a later section, the presence of the droplet causes the disruption of uniform plasma emission, and thus, greatly affects the quality of the ionic wind. It is believed that this has a direct effect on the heat dissipation of the actuator. However, further studies are needed to understand the extent of heat dissipation by the induced airflow.

The role of water in the dielectric barrier discharge

Water may take the role of either the anode producing glow discharges or the cathode producing streamer discharges under DC excitation[43]. Water as a liquid electrode has also been investigated in AC voltages, in which it alternates between the roles of anode and cathode[44,45]. It was found that the plasma discharge initiates at the water surface and that it exhibits distinct features depending on the polarity[45].

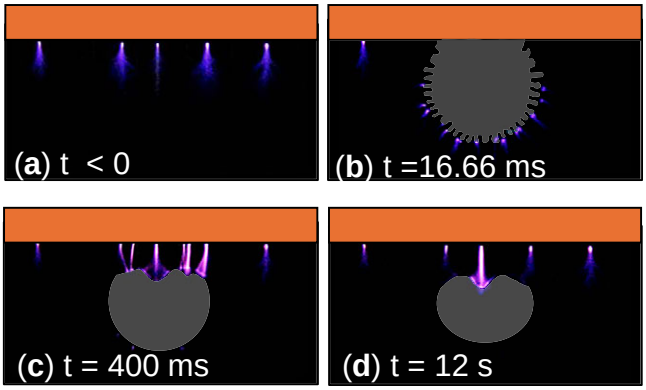

Fig. 5 | Droplet-plasma interactions upon impingement. Color imaging of plasma emission (**a**) attached to electrode edge prior to droplet impact, (**b**) at the tips of the finger structures after droplet spreading, (**c**) as multiple streamers between the electrode and the base of the droplet during separation, and (**d**) as a single streamer between the electrode and the droplet.

The roles of water in the plasma emissions through the various stages of droplet spread, separation, and evaporation are discussed in this section. Figure 5 and the Supplementary Video 2 show the emissions observed through color photography (at a frame rate of 60 fps and with an exposure time of 1/60 s) in the four stages described above. Figure 5a shows the plasma emission from the edge of the electrode prior to droplet impact. A few concentrated specks are observed propagating a few millimeters away from the electrode.

During the spreading phase depicted in Fig. 5b, the water droplet maintains contact with the exposed electrode and thus takes the role of a liquid electrode[19,22,43,44]. Charges are transferred from the electrode to the droplet and accumulate at the regions of smaller radii of curvature (fingertips). This accumulation of charges ionizes the air around the fingertips, giving rise to localized plasma emissions. Emphasis is made in the fact that these discharges occur at the tips of the liquid fingers rather than between the fingers as reported in Hele-Shaw cells by Hou and Chu[46], and by Chu and Lee[47]. Qualitatively, these discharges have the same appearance as those in Fig. 5a, however the thermal signatures left by the fingertip emissions are not as intense as those emanating from the solid electrode, as pointed out in the discussion for Fig. 3b, likely due to their transient nature.

As the base of the droplet heats up and evaporates, the liquid separates from the metallic electrode. The water then assumes the role of the ground electrode and plasma filaments form between the droplet and the electrode as shown in Fig. 5c, d. It is pointed out that in the case presented in Fig. 5, we did not observe the formation of secondary droplets and secondary streamers described in the previous section. Further, this case displayed an earlier separation from the electrode compared to Fig. 3. For instance, the primary streamers are visible in Fig. 5c at 400 ms after impact while they appear only after one second, as suggested by the thermal images in Fig. 3 and the temperature plots in Fig. 4. These discrepancies in the system response can be due to variations in the surface temperature at the moment of droplet impact, to the degree of plasma treatment of the dielectric surface (varying surface roughness and wettability), or by the stochastic nature of droplet spreading after impact.

During the stage of droplet separation, the streamers drive the liquid's evaporation at the base of the droplet. As mentioned earlier, a memory effect was observed as the streamers repeatedly appeared at one location. This results in a growing indentation at the base of the droplet (at the point of contact of the streamer in Fig. 5d) caused by the disproportionate evaporation at a hot spot and by the body force

applied to the liquid. The evolution of the indentation is pointed out in the Supplementary Video 2. The memory effect of the streamer at the indentation combined with the relatively long exposure time (1/60 s) of the camera produces an optical illusion seen in Fig. 5c, d that should be elucidated. Every frame captured by the camera encompasses roughly 167 AC cycles, and thus the generated image is the superposition of the multiple streamers. This can result in the illumination of several regions within the same frame. In particular, a streamer branching effect is seen around the droplet indentation, where the base and the stem of the streamer remain fixed but its tip is deflected to contact the liquid at various locations within the indentation, resulting in various apparent ramifications. Further, a uniformly distributed glow develops along the wall of the indentation, giving the appearance of an arrow. An additional noteworthy phenomenon observed in the video is the penetration of some of the more intense streamers into the liquid. This is evident in the early stage of droplet separation both in the indentation and in the periphery of the droplet. Streamer penetration into the liquid phase could be the cause of some of the thermal features discussed in the previous section.

Upon formation of secondary droplets, a network of streamers may form connecting the various droplets to the exposed electrode. That is, single or multiple streamers form between the electrode and the primary droplet. Additional streamers then form from the opposite side of the primary droplet and extend to reach nearby secondary droplets. Similar effects were reported by Lilley et al.[27]. for DBD actuators operating with multiple droplets on their surfaces, where a thin region of water remained in contact with the exposed electrode and the network of streamers formed between this layer of water and the isolated droplets.

Droplet spreading and development of finger instability

A particular feature of droplet impact is the development of finger structures along the spreading rim. Thoroddsen and Sakakibara[48] conducted an in-depth analysis of this fingering instability on water droplets of comparatively higher inertia than those of this study (Re ~ 15,000 and We ~ 1000) impacting a glass surface. Our experimental results using water droplets of relatively low inertia ($d_o \approx 2.76$ mm, Re = 7000, and We = 250) suggest that the presence of plasma promotes a higher degree of droplet spreading as well as the formation of well-defined slender finger structures. This is illustrated by photographs taken at 4,000 fps and with an exposure time of 1/4,000 s in Fig. 6, where spreading is compared for a droplet impacting the plasma-treated PMMA surface of the actuator in the absence of plasma (no electric field acting on the droplet), as shown in Fig. 6a, b, and a droplet impacting on the same surface during plasma actuation, as shown in Fig. 6c, d. It is important to highlight that the surface had previously been treated with plasma even in the "Plasma off" case, which has significant effects on surface wettability, as previously shown in Fig. S1. The photographs in Fig. 6a, c illustrate the droplets at the moment of impact ($t = 0$) as well as at the moment of maximum spreading at $t = 3$ ms for the case with no plasma and $t = 7$ ms when the plasma is on. Here, we define the time to maximum spreading based on the outer diameter. The inner (d_{in}) and outer (d_{out}) diameters of the droplets are approximated with the red and blue superimposed circles, respectively. The time evolution of d_{in} and d_{out} normalized by d_o, as well as the normalized average finger length ($l_f = (d_{out} - d_{in})/d_o$, in black triangles) are given in Fig. 6b, d for plasma off and on, respectively.

It is noted from these two plots that in both cases the fingers appear ~ 1 ms after impact. However, the finger length remains relatively constant in the case with plasma off, while it increases almost monotonically when the plasma is on. It is noted that the behavior of the inner diameter (in red squares) is similar regardless of the presence of plasma. In both instances, the values of d_{in} seem to plateau at $t \approx 3$ ms, which coincides with the time of maximum spreading in the case of plasma off. In addition, receding waves (such as those seen in frame (c) at $t = 7$ ms) begin to form at the rim and propagate inward. We determine that the inertial effect of the droplet spread ends when d_{in} plateaus. Further, l_f slightly decreases after the maximum spreading of the droplet in the absence of plasma. The formation of small fingers ($l_f / d_o = 0.15$) prior to maximum spreading in the absence of plasma results from the imbalance between inertial and capillary forces. The instability does not grow in time since the inertial effects die out after maximum spreading.

On the other hand, the case with plasma exhibits finger growth during and after inertial effects. A direct comparison between the two cases indicate that the finger growth rate during the inertial spreading is higher in the presence of plasma. This suggests that other forces are involved besides inertial. In fact, we observe that a bright plasma streamer forms between the electrode and the liquid at the moment of impact, as shown in Fig. 6e. The streamer formation is a nanosecond process which takes place within the positive half of the AC cycle[4]. This initial streamer serves as a bridge through which a large number of charges are transferred to the droplet. The droplet then is subjected to Coulomb forces radially outward resulting from the redistribution of charges. These forces are however circumferentially uneven due to the external electric field caused by the electrode, resulting in a variation in finger length, where the fingers farther from the electrode are longer than those in its proximity. The added momentum to the initial spreading of the droplet favors the destabilization of the spreading front of the droplet and promotes the finger formation.

An additional effect of the plasma on the droplet spreading and the fingering phenomenon is an increased wettability of the dielectric surface. The surface wettability can be characterized by the degree of spreading, which is dictated by the spreading parameter $S = \gamma_{SA} - \gamma_{SL} - \gamma_{LA}$, defined by the surface tensions for the surface-air (SA), surface-liquid (SL), and liquid-air (LA) interfaces. The spreading parameter S increases with plasma intensity, i.e., towards the electrode, opposing the electric field as shown in Fig. 6f. However locally at the fingertips, the gradient of S is directed radially outward as a result of the plasma ejections at the spreading front as shown in Fig. 5b. It is noted that the presence of these localized glow discharges originating from the tips of the developing finger structures, visible prior to the main droplet separation (Fig. 5b, Supplementary Video 2) and schematically depicted in Fig. 6f, are deemed to play a key role in locally reducing surface tension at the finger tips and in enhancing the dielectric surface's wettability. This process enables the development of more pronounced and well-defined fingering structures during the first ~ 10 ms, before bulk thermal effects or secondary streamer activity become significant. Further, the uneven heating of the droplet at the solid-liquid interfacial layer induces thermal Marangoni flows away from the electrode and radially outward. The applied voltage on the electrode as well as the presence of plasma induce charges on the dielectric material, increasing its wettability through a process known as electrowetting[49–51]. Quetzeri-Santiago et al.[51]. demonstrated the use of dielectrowetting to manipulate the dynamics of droplet impact.

To further illustrate the coupled inertial and electrically-induced effects on the development of the fingering instability, the experiment was repeated with the droplet spreading fully on the dielectric as presented in Fig. S2 in the Supplementary Material and in the Supplementary Video 3. In this case, the center of the 2.75 mm droplet impacts at an offset of 10.3 mm away from the edge of the electrode and is thus, initially not acted upon by the plasma. The sequence of images (taken at 3000 fps and with exposure time of 1/3,000 s) reveals that as the advancing rim approaches the exposed electrode (at the top of the image), a single plasma streamer highlighted in red develops between the electrode and the nearest part of the droplet at $t = 1.66$ ms. Until then, the spread of the droplet appears to be nearly symmetrical with evenly distributed fingers developing around its circumference. After the initial contact, the streamer intensifies (seen

https://doi.org/10.1038/s41467-025-64991-x

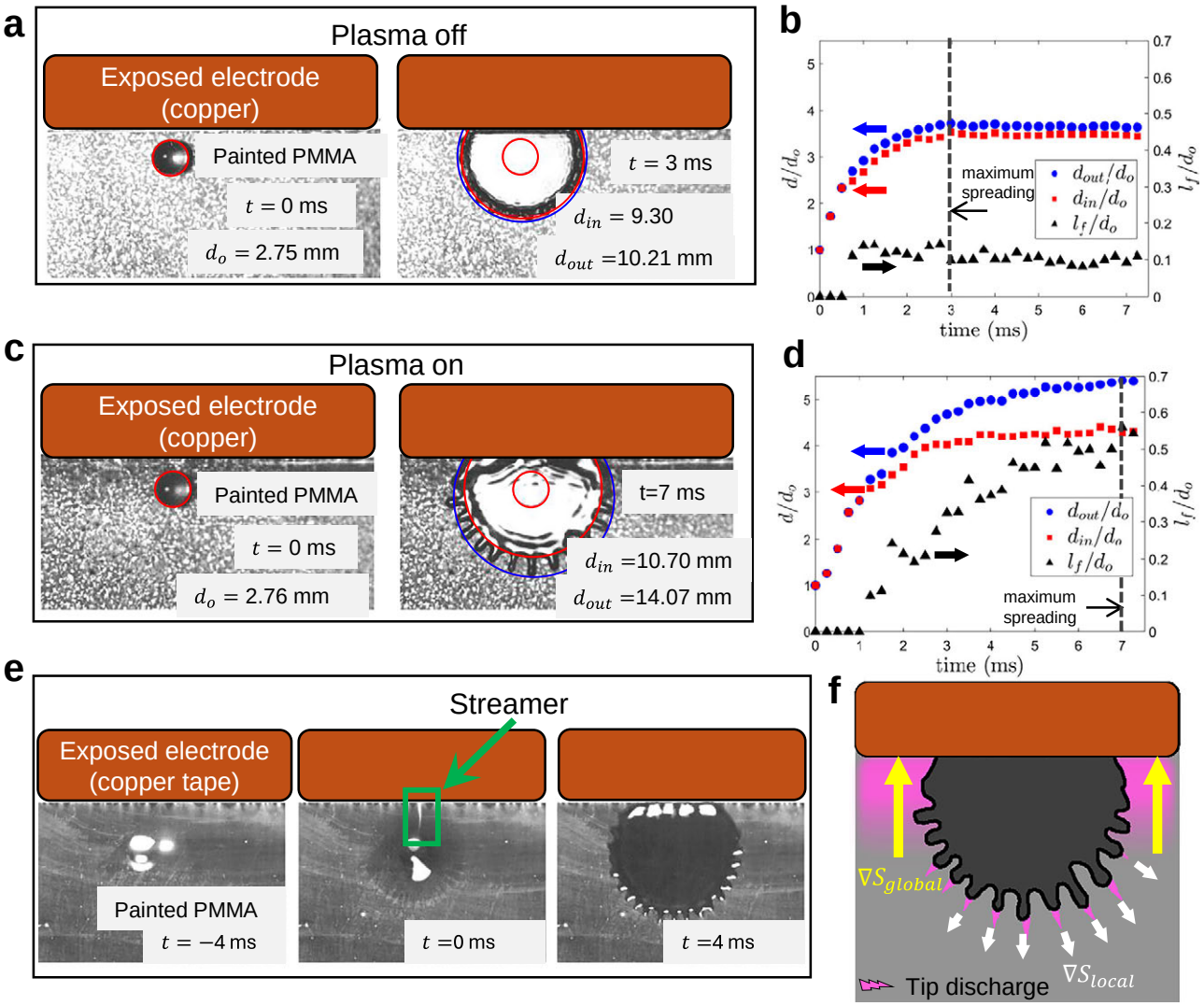

Fig. 6 | Onset of fingering instability on spreading droplet. Droplet spreading over the PMMA dielectric surface. Images taken at 4000 fps and with exposure time of 1/4000 s. **a** High-speed images of droplet at the moment of impact and at the maximum spreading in the absence of plasma. **b** Temporal evolution of the normalized droplet inner and outer diameters, and the finger length in the absence of plasma. **c** High-speed images of droplet at the moment of impact and at the maximum spreading with a plasma discharge. **d** Temporal evolution of the normalized droplet inner and outer diameters, and the finger length with plasma discharge. **e** Streamer formation between electrode and droplet at moment of impact imparts charges to the droplet. Coulomb forces are induced under the effect of electric field. **f** Schematic of global and local wettability gradients ∇S on the dielectric surface promote the growth of finger instability.

as a white streak), penetrates into the liquid film (see frame at t = 3 ms), and makes an indentation at the point of contact with the droplet. The streamer then remains relatively stable at said location and is only deflected at the tip, contacting the liquid at different points along the contour of the indentation. Such indentations were already presented in Fig. 5 and in the Supplementary Video 2, with the streamer recurrently forming at certain locations. Furthermore, by coupling the observations in Fig. S2 with the geometric shift between the blue and red circles in Fig. 6c, we highlight the combined influence of plasma-induced surface modification and polarization field effects on the asymmetric development of finger lengths. The plasma activity not only alters the local surface properties but also modifies the electric field distribution, leading to preferential growth directions that produce the observed asymmetry. It is also worth mentioning that, electric field–induced polarization alone can also influence the fingering dynamics. Although polarization in the absence of plasma is insufficient to fully reproduce the pronounced finger asymmetry and stabilization observed under plasma activation, our supplementary tests indicate that it still makes a measurable contribution to variations in finger length. For more details on these observations and the associated comparison between electric field only, no electric field, and plasma-on cases, readers are referred to the discussion provided in the Supplementary Material for Fig. S3.

The snapshots in Fig. S2 and the accompanying Supplementary Video 3 also suggest that the plasma streamer penetrates into the liquid droplet. This penetration mechanism can be responsible for some of the well-defined thermal signatures within the liquid droplet found in Fig. 3c, e. The top-view of these images, however, cannot be used to conclusively determine the depth of the streamer location with respect to the droplet's profile. That is, whether the streamer lies on the droplet surface, along the interface of the droplet and the dielectric surface, or somewhere in between, fully embedded into the liquid. Further investigation is then needed to elucidate the question of streamer trajectory after penetrating into the liquid film.

It should also be noted that, under typical atmospheric conditions, the thin air layer between an approaching droplet and the

https://doi.org/10.1038/s41467-025-64991-x

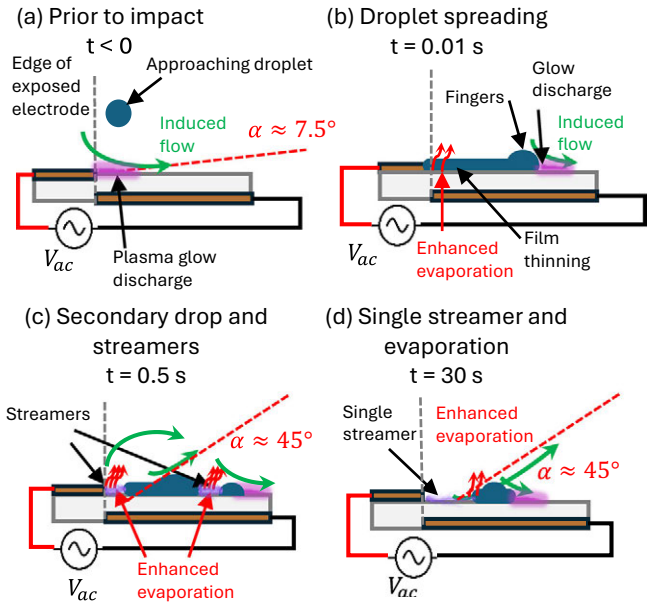

Fig. 7 | Disturbance of ionic wind induced by droplet impact. Schematic representation of the effects of droplet impact on the induced flow at the above mentioned stages. (**a**) Prior to droplet impact, the steady induced flow is almost parallel to the dielectric surface, with slight divergence in the downstream; (**b**) Upon droplet impact and spreading, the initial flow is disrupted, with the induced flow generated at the fingertips of the spreading droplet; (**c**) Secondary droplet formation and primary/secondary streamer production, with more complex induced flow from both the electrode and droplet edges; (**d**) Steady single streamer formation between the electrode and the droplet, along with the complex three-dimensional flow caused by the bleeding of surrounding airflows.

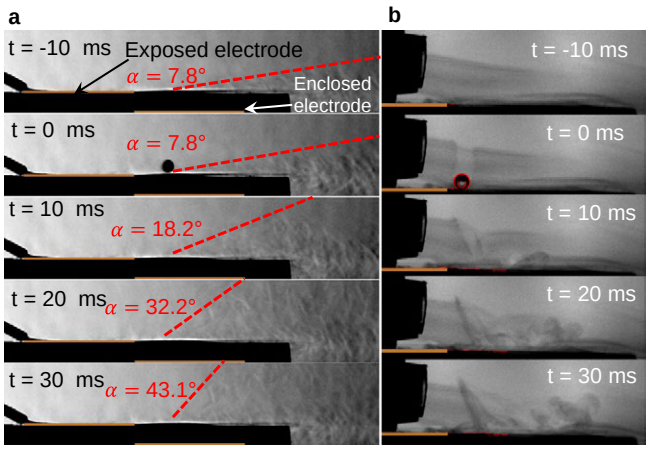

Fig. 8 | Dynamic response of the ionic wind to droplet impact. a Schlieren imaging reveals an increase in the angle α that the induced airflow forms with the dielectric surface. **b** Flow visualization by mist addition denote turbulent flow structures formed over the spreading droplet (marked in red) which propagate downstream. The envelope of turbulent structures correspond to the measurements of α in (**a**).

substrate also plays a critical role in determining impact outcomes including the spreading and fingering features. In the present study, the surface DBD plasma introduces a partially ionized zone near the substrate, which can locally modify the thermophysical properties of the surrounding gas. While the overall degree of ionization in atmospheric-pressure DBD plasma remains low, localized gas heating and charge-induced transport can alter both the density and viscosity of the air layer just prior to impact. This may result in thermal thinning of the gas cushion, potentially suppressing the air cushioning effect and promoting earlier contact between the droplet and surface. Additionally, electrohydrodynamic forces induced by the plasma may accelerate the air and deform the gas-liquid interface, further influencing the impact dynamics. Although a detailed quantification of these effects requires dedicated diagnostics and modeling beyond the scope of this study, the observed enhancement in droplet spreading and altered wetting behavior in the presence of plasma are consistent with such localized modifications of the gas layer.

Effects on the induced airflow

One of the effects of droplet impact on the surface plasma is a notable disruption of the ionic wind stream. As discussed earlier, the reliability in the formation of a steady flow has been the subject of multiple studies for flow control applications[3–6]. Some studies have reported a reduction of thrust in DBD actuators in the presence of water droplets[27] and at high levels of humidity[28]. However, to the best of our knowledge, the transient effects on the ionic wind in the presence of water droplets has not been documented. Based on the previous discussion, we identify three mechanisms responsible for the disruption of the flow: disruptions of the plasma discharge, physical blockage by the droplet, and thermal effects. Here, we present the disruptions on the induced flow following droplet impact. Our observations are schematically presented in Fig. 7. Further, experimental results are presented in Fig. 8 using (a) Schlieren, and (b) flow visualization by adding mist to the flow.

The initially steady airflow is disrupted as soon as the droplet impacts and spreads over the dielectric surface. During this early stage, the droplet plays the role of an extended electrode and the glow plasma emissions take place at the droplet's fingertips (as illustrated in Fig. 5b and Supplementary Video 2). This modifies both the location and direction of the plasma discharge. That is, the emission is no longer at the electrode edge and perpendicular to it. Instead, the plasma is emitted at the periphery of the droplet and is directed radially outward from its center. The induced airflow then conforms to the modified emission pattern, as schematically illustrated in Fig. 7b.

As the base of the droplet evaporates and high-temperature streamers form, thermal effects become more dominant on the gas phase as shown in Fig. 7c, d. The formation of streamers induces a body force on the air above them. The induced airflow is however much more disturbed compared to the flow generated in the absence of the droplet. Further, the induced flow over the liquid film is three-dimensional, and the airflow generated elsewhere along the electrode edge may bleed over the droplet.

To reveal the transient flow structure evolution during the early stage of this process (i.e., within the first 30 ms following droplet impact), high-speed Schlieren images shown in Fig. 8a were acquired at 10,000 fps and exposure time of 1/35,000 s, providing a close observation of the gas dynamics surrounding the region of droplet-plasma interactions. The wall jet is seen to originate from the edge of the exposed actuator. The flow structures seen in the Schlieren images are found to have a diverging angle with respect to the dielectric surface, $\alpha = 7.8°$ prior to droplet impact.

As the water droplet impacted on the dielectric surface of the actuator near the exposed electrode, the angle α rapidly increased. This is illustrated in Fig. 8 which shows five frames at intervals of 10 ms from $t = -10$ ms to $t = 30$ ms. α increases from 7.8° at $t = 0$ to 43.1° at $t = 30$ ms for a $\Delta\alpha = 35.3°$. It is worth noting that, the alterations in the flow field observed in the Schlieren images (Fig. 8) roughly correspond to the stage of droplet spreading.

It is recognized that the flow structures captured with Schlieren imaging are essentially caused by the gas density variation (temperature variation) in the vicinity of the droplet-plasma interaction region. During the plasma discharge, the localized heating and its interplay with the rapidly spreading droplet created a highly three-dimensional

thermal plume structure, which is carried downstream by the induced flow. While the Schlieren imaging comprises the integral of the flow along the entire span of the plasma actuator, it is believed that the variation in the flow structures is primarily caused by the thermal and dynamic disturbances in the region of the droplet impact, as seen in Fig. 8.

The flow pattern over the droplet was also investigated by injecting a stream of fine water mist directly upstream of the region of impact. The velocity of the mist was deemed to be much smaller than that of the induced jet and can be neglected. A series of high-speed, back-illuminated images taken at a rate of 12,000 fps and with an exposure time of 1/70,000 s is presented in Fig. 8b. The frames in the figure show the end of the mist delivery tube from which the fine mist is ejected from the left side. The tube is placed over the exposed electrode (indicated in bronze color). The contour of the droplet prior to impact and as it spreads over the surface was detected through a Sobel filter and is highlighted in red. The first frame illustrates the stream of mist coming out of the tube before the droplet impact ($t = -10$ ms). The second frame ($t = 0$) shows the moment of the droplet impacting the dielectric surface. The wake of the droplet is observed as it cuts through the mist. The flow elsewhere is undisturbed. Within the first 10 ms, the droplet has spread on the surface. A flow structure emerges from the advancing edge of the droplet marked in red. This is likely the new induced jet caused by the glow plasma discharge at the edge of the droplet. Once the droplet stops spreading (that is, during the fourth and fifth frames in Fig. 8b), turbulent flow structures form directly over the droplet and are seen to propagate downstream. Since the droplet acts as an extended electrode and the flow is generated only at the edge of the drop, where the glow plasma discharge occurs, it is not expected to observe any flows generated directly over the droplet. However, due to the highly three-dimensional flow in the vicinity of the droplet-plasma interaction region, where the induced flows generated along the adjacent electrode bleed over the edge of the droplet, the hot induced airflow gets deflected as it jumps over the edge of the droplet. Further, it mixes with the cool air directly above the droplet surface. This results in the turbulent structures observed at $t = 20$ and 30 ms, which is responsible for the rapid change in the angle α.

Discussion

Our experimental investigation uncovers the intricate dynamics arising from the interaction between an impinging water droplet and a plasma-covered dielectric surface within an AC-DBD system. This multiphase environment, comprised of solid, liquid, gas, and plasma, exemplifies a highly complex regime where charge, mass, and energy are exchanged across disparate phases within microsecond-to-second timescales. The results elucidate fundamental physical mechanisms that govern the behavior of droplets in plasma-exposed environments and carry broader implications for plasma-assisted technologies in aerospace, environmental, and biomedical fields.

One of the key findings of this study is the significant enhancement in droplet spreading and fingering, which is directly attributed to the plasma-induced modifications in solid surface and liquid properties. This phenomenon, commonly associated with transient modifications in surface energy caused by plasma exposure, facilitates a rapid outward motion of the contact line. Superimposed on this spreading is the emergence of finger-like instabilities at the droplet periphery, an important feature of the interplay between capillary, inertial, and plasma-induced electrohydrodynamic forces. In addition to these plasma effects, electric field–induced polarization, even in the absence of plasma, is found to contribute measurably to the variations in finger length, although it alone cannot fully reproduce the pronounced asymmetry observed under plasma activation. The detailed Schlieren imaging further reveals density gradients indicative of localized thermal variations due to the plasma-induced heating and evaporative cooling.

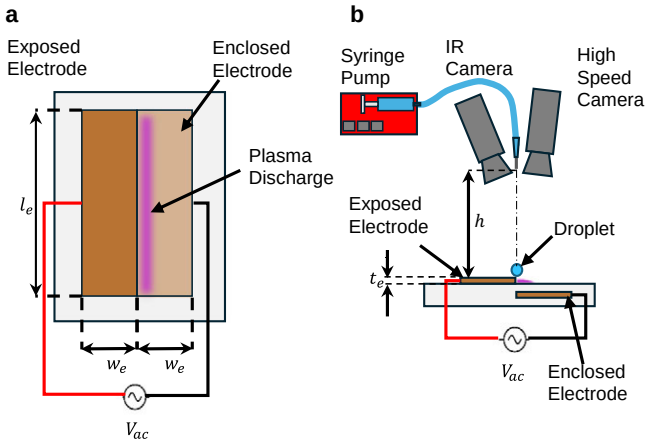

Fig. 9 | Experimental setup. a Schematic and dimensions of the surface DBD actuator. **b** Schematic of the experimental setup.

The formation of localized micro-discharges at the liquid-solid-gas interfaces represents another notable observation, suggesting the presence of transient triple-phase boundary dynamics that add complexity to the plasma discharge behaviors. These early-stage glow discharges, distinct from the later-developed secondary streamers, are confined to the vicinity of finger tips, where they enhance localized energy deposition and promote evaporation. This process reduces the local surface tension at the finger tips and increases the dielectric surface's wettability, enabling the early development of more pronounced and well-defined fingering structures. Simultaneously, we observe disruption in the DBD-induced ionic wind upon droplet impact. This temporary collapse of the induced flow field demonstrates the sensitivity of near-wall plasma actuators to droplet impingement, which has direct consequences for their application in active flow control. Thermal imaging and time-resolved visualizations suggest that plasma-induced heating plays a dual role: it enhances evaporation while concurrently modifying the interfacial dynamics. These coupled thermal and electrostatic effects challenge the common assumption of phase independence in such multiphase systems and necessitate the development of new models that account for temporally evolving interfacial properties.

From an applied perspective, the insights gained here have immediate relevance to technologies involving droplet-plasma interactions. For instance, in the context of plasma-based de-icing, the enhanced spreading and localized evaporation may support more effective energy distribution across ice-contaminated surfaces. Similarly, in biomedical or disinfection applications, the complex interface dynamics and local heating effects may alter how active species are delivered to or interact with biological matter.

Methods

Dielectric barrier discharge actuators

The DBD actuator used in this study consisted of two electrodes: one exposed to the air, and the second one encapsulated by the dielectric material. Figure 9 offers (a) a top and (b) a side view of the actuator with its relevant dimensions. The electrodes were made out of copper tape of thickness $t_e = 0.1$ mm, the width and length of the electrodes were $w_e = 25.4$ mm, and $l_e = 60$ mm, respectively. The electrodes were positioned asymmetrically so that there was no gap between them ($d_e = 0$). The dielectric material was acrylic (polymethyl methacrylate, PMMA) with a thickness $t_d = 5.25$ mm between the two electrodes. The top surface of the PMMA was coated with a black enamel spray paint to improve the emission properties of the acrylic for the purposes of

infrared imaging. The two electrodes were connected to a high-voltage AC source (CTP-2000K, Nanjin Suman Plasma Technology Co.) used to generate a non-equilibrium plasma discharge on the surface of the dielectric material. The power supply provided a high-voltage sinusoidal signal of controllable voltage and frequency. For the current study, these parameters were fixed at $V_{pp} = 25$ kV and $f = 10$ kHz, respectively.

Experimental setup

The experimental setup is schematically shown in Fig. 9(b). Single droplets of distilled water of electrical conductivity 8 − 9 μS/cm were released 40 cm above the surface of the actuator using a syringe pump (NE-1000, New Era Pump Systems, Inc., Farmingdale, NY) through a stainless steel needle (30 gauge). The liquid was driven at a constant rate of 0.1 mL/min in all experiments. Droplets slowly formed at the needle tip and detached by gravity, yielding a consistent droplet size ($d = 2.75$ mm) in all experiments. The needle was aligned to the edge of the exposed electrode where the sheet of plasma was generated.

Thermal infrared (IR) and high-speed (HS) cameras were synchronized to simultaneously record the thermal and dynamic behaviors of the droplet impacting the surface with plasma. The IR (FLIR A600-Series, FLIR, Täby, Sweden) and HS (FASTCAM Nova R3-4K, Photron USA, Inc., San Diego, CA) cameras were mounted at the same level of the tip of the needle, to capture the top view of the processes. The infrared images were acquired at a frame rate of 200 fps and exposure time of 1/200 s with a spatial resolution of 640 × 120 pixels, yielding a magnification of 22.22 μm per pixel. The camera was controlled, and images were processed with the software IR research (FLIR, Täby, Sweden). To ensure accurate temperature measurements with the IR camera, a calibration procedure was conducted to correlate the camera's output count number, which is directly related to the infrared radiation received from the surface, with the actual surface temperature. This calibration accounted for key influencing factors, including the working distance, ambient temperature, and the emissivity values of the materials involved (i.e., the black-painted dielectric surface and the water droplet) as demonstrated in several previous studies[7,8,52]. Notably, under isothermal conditions, the black-coated surface and the water droplet exhibited the same IR count values, indicating that they have effectively the same emissivity within the measurement range. This observation is consistent with literature-reported emissivity values: the black coating provides a well-defined emissivity of approximately $\varepsilon = 0.95$, while water droplets are known to have emissivity values in the range of $\varepsilon = 0.95 - 0.98$ in the 8 − 14 μm spectral window of the IR camera[52]. As such, the same calibration curve was applied for both object materials to convert IR counts into temperature values. It should be noted that dielectric barrier discharge (DBD) plasma may cause changes in surface chemistry and micro-/nano-structures due to oxidation or surface functionalization (e.g., the introduction of OH or COOH groups). As shown in previous studies[12,53,54], plasma–dielectric interactions can modify the dielectric's impedance and local electric field through heating and surface charge effects, thereby altering the electrical and thermal properties of the dielectric materials. However, it is believed that these effects are typically moderate, and are not expected to significantly influence the qualitative thermal trends reported.

The high-speed camera was operated at frame rates varying from 2000 to 4000 fps and corresponding exposure times of 1/2000 to 1/4000 s, depending on lighting conditions with a resolution of 20.44 μm per pixel. A UV lens (UV-Nikkor 105 mm F4.5, Nikon, Japan) with high transmittance rate (~70%) was attached to the camera to capture plasma structures such as the high intensity streamers. Alternatively, a color video camera (Canon Rebel T7, Canon) was placed to record the plasma discharges around the droplet at 60 fps and with an exposure time of 1/60 s.

A simple Z-type Schlieren configuration was utilized to obtain the side view of the plasma actuator and the induced airflow (in Fig. 8). The Schlieren system consisted of a green LED light source emitting from a pinhole, two parabolic mirrors of 203.2 mm in diameter and a focal length of $f/8$, a knife edge, and a high speed camera (FASTCAM Nova R3-4K, Photron USA, Inc., San Diego, CA). Images were taken at a frame rate of 10,000 fps, with spatial resolution of 2048 × 256 pixels, and an exposure time of 1/35,000 s. A 400 mm lens was used, yielding a magnification of 57 μm per pixel. Images for flow visualization by mist addition were acquired at 12,000 fps and at an exposure time of 1/70,000 s. The deflection angles (α) of the induced flow were obtained through detailed image processing of the high-speed Schlieren image sequences. Local flow disturbances were determined by tracking the distinct flow features, quantified via the standard deviation of pixel intensity within a 3 × 3 pixel neighborhood. This approach effectively captures the enhanced turbulence and structural variations in the flow as it is deflected by the impinging droplet. Based on repeated measurements and the spatial resolution of the imaging system, the uncertainty in α was estimated to be ± 0.1°.

In all experiments, the droplet diameters were calculated from the magnification rates reported above. The inner and outer spreading diameters (d_{in} and d_{out}), as well as the average finger length (l_f) reported in Fig. 6 were measured in a similar manner at each frame of the high-speed images during the spreading stage ($dt = 0.25$ ms). Images were processed using an in-house built MATLAB routine based on edge detection and image segmentation to extract droplet size, shape, and location. The description of the algorithm and its uncertainty quantification showing <1% of error in droplet measurement have been presented in previous publications[55,56]. The droplet impact velocity was calculated as $V = 2.55$ m/s by tracking the droplet's centroid location in high-speed images. The non-dimensional numbers of relevance for droplet impact were calculated as We = 250, Re =;7000, Oh = 0.0023, and Ca = 0.036.

Data availability

All datasets supporting the findings of this study are available in Figshare: Source Data[57].

References

1. Bogaerts, A., Neyts, E., Gijbels, R. & van der Mullen, J. Gas discharge plasmas and their applications. *Spectrochimica Acta Part B: At. Spectrosc.* **57**, 609–658 (2002).
2. Massines, F., Sarra-Bournet, C., Fanelli, F., Naudé, N. & Gherardi, N. Atmospheric pressure low temperature direct plasma technology: Status and challenges for thin film deposition. *Plasma Process. Polym.* **9**, 1041–1073 (2012).
3. Corke, T. C., Post, M. L. & Orlov, D. M. Single dielectric barrier discharge plasma enhanced aerodynamics: Physics, modeling and applications. *Exp. Fluids* **46**, 1–26 (2009).
4. Benard, N. & Moreau, E. Electrical and mechanical characteristics of surface ac dielectric barrier discharge plasma actuators applied to airflow control. *Exp. Fluids* **55**, 1846 (2014).
5. Corke, T. C., Enloe, C. L. & Wilkinson, S. P. Dielectric barrier discharge plasma actuators for flow control. *Annu. Rev. Fluid Mech.* **42**, 505–529 (2010).
6. Zhang, X., Cui, Y. D., Tay, C. M. J. & Khoo, B. C. Flow field generated by a bielectric barrier discharge plasma actuator in quiescent air at initiation stage. *Chin. J. Aeronautics* **34**, 13–24 (2021).
7. Liu, Y., Kolbakir, C., Hu, H. & Hu, H. A comparison study on the thermal effects in dbd plasma actuation and electrical heating for aircraft icing mitigation. *Int. J. Heat. Mass Transf.* **124**, 319–330 (2018).
8. Liu, Y., Kolbakir, C., Hu, H., Meng, X. & Hu, H. An experimental study on the thermal effects of duty-cycled plasma actuation pertinent to aircraft icing mitigation. *Int. J. Heat. Mass Transf.* **136**, 864–876 (2019).

9. Cai, J. et al. An experimental study of icing control using dbd plasma actuator. *Exp. Fluids* **58**, 1 (2017).
10. Stanfield, S. A., Menart, J., DeJoseph, C., Kimmel, R. L. & Hayes, J. R. Rotational and vibrational temperature distributions for a dielectric barrier discharge in air. *AIAA J.* **47**, 1107–1115 (2009).
11. Dong, B., Bauchire, J. M., Pouvesle, J. M., Magnier, P. & Hong, D. Experimental study of a dbd surface discharge for the active control of subsonic airflow. *J. Phys. D: Appl. Phys.* **41**, 155201 (2008).
12. Zhang, X., Zhao, Y. & Yang, C. Recent developments in thermal characteristics of surface dielectric barrier discharge plasma actuators driven by sinusoidal high-voltage power. *Chin. J. Aeronautics* **36**, 1–21 (2023).
13. Rodrigues, F., Pascoa, J. & Trancossi, M. Heat generation mechanisms of dbd plasma actuators. *Exp. Therm. Fluid Sci.* **90**, 55–65 (2018).
14. Gulyaev, I. Phenomenological model of the suspension droplets evaporation in a plasma flow considering different mass transfer mechanisms. *Surf. Coat. Technol.* **404**, 126454 (2020).
15. Stancampiano, A. et al. Plasma and aerosols: Challenges, opportunities and perspectives. *Appl. Sci.* **9**, 3861 (2019).
16. Bruggeman, P. J. et al. Plasma–liquid interactions: a review and roadmap. Plasma. *Sources Sci. Technol.* **25**, 053002 (2016).
17. Xie, H. et al. A stable atmospheric-pressure plasma for extreme-temperature synthesis. *Nature* **623**, 964–971 (2023).
18. de Groot, G. J. J. B., Hundt, A., Murphy, A. B., Bange, M. P., and Mai-Prochnow, A. Cold plasma treatment for cotton seed germination improvement. *Scientific Rep.* **8**, 14372 (2018).
19. Vanraes, P. & Bogaerts, A. The essential role of the plasma sheath in plasma–liquid interaction and its applications—a perspective. *J. Appl. Phys.* **129**, 220901 (2021).
20. Adamovich, I. et al. The 2017 plasma roadmap: Low temperature plasma science and technology. *J. Phys. D: Appl. Phys.* **50**, 323001 (2017).
21. Samukawa, S. et al. The 2012 plasma roadmap. *J. Phys. D: Appl. Phys.* **45**, 253001 (2012).
22. Vanraes, P. and Bogaerts, A. Plasma physics of liquids - a focused review. *Appl. Phys. Rev.* **5**, 031103 (2018).
23. Lehocký, M. et al. Plasma surface modification of polyethylene. *Colloids Surf. A: Physicochem. Eng. Asp.* **222**, 125–131, (2003).
24. Han, S. et al. Polymer surface modification by plasma source ion implantation. *Surf. Coat. Technol.* **93**, 261–264 (1997).
25. Morent, R., De Geyter, N., Desmet, T., Dubruel, P. & Leys, C. Plasma surface modification of biodegradable polymers: A review. *Plasma Process. Polym.* **8**, 171–190 (2011).
26. Wen, Q. et al. Negative effects of sdbd plasma anti-/de-icing method for wind turbine blades. *Appl. Surface Sci.* **688**, 162341 (2025).
27. Lilley, A. J., Roy, S., Michels, L. & Roy, S. Performance recovery of plasma actuators in wet conditions. *J. Phys. D: Appl. Phys.* **55**, 155201 (2022).
28. Wicks, M. & Thomas, F. O. Effect of relative humidity on dielectric barrier discharge plasma actuator body force. *AIAA J.* **53**, 2801–2805 (2015).
29. Worthington, A. M. On the forms assumed by drops of liquids falling vertically on a horizontal plate. *Proc. R. Soc. Lond.* **25**, 261–272 (1877).
30. Josserand, C., Thoroddsen, S. T. T., Josserand, C. & Thoroddsen, S. T. Drop impact on a solid surface. *Annu. Rev. Fluid Mech.* **48**, 365–391 (2016).
31. Rein, M. Phenomena of liquid drop impact on solid and liquid surfaces. *Fluid Dyn. Res.* **12**, 61–93 (1993).
32. Park, H. Y., Kang, B. J., Lee, D. & Oh, J. H. Control of surface wettability for inkjet printing by combining hydrophobic coating and plasma treatment. *Thin Solid Films* **546**, 162–166 (2013).
33. Carrino, L., Moroni, G. & Polini, W. Cold plasma treatment of polypropylene surface: a study on wettability and adhesion. *J. Mater. Process. Technol.* **121**, 373–382 (2002).
34. Schuman, T. & Wolf, R. A. Effects of a dbd plasma discharge on bond strength. *Surf. Interfaces* **18**, 100461 (2020).
35. Assael, M. J., Botsios, S., Gialou, K., and Metaxa, I.N. Thermal conductivity of polymethyl methacrylate (pmma) and borosilicate crown glass BK7. *Int. J. Thermophysics* **26**, 1595–1605 (2005).
36. Wong, K. S., Chew, N. S. L., Low, M., and Tan, M. K. Plasma-activated water: Physicochemical properties, generation techniques, and applications. *Processes* **11**, 2213 (2023).
37. Hu, H. & Larson, R. G. Evaporation of a sessile droplet on a substrate. *J. Phys. Chem. B* **106**, 1334–1344 (2002).
38. Deegan, R. D. Pattern formation in drying drops. *Phys. Rev. E* **61**, 475–485 (2000).
39. David, S., Sefiane, K. & Tadrist, L. Experimental investigation of the effect of thermal properties of the substrate in the wetting and evaporation of sessile drops. *Colloids Surf. A: Physicochem. Eng. Asp.* **298**, 108–114 (2007). XVIIth European Chemistry at Interfaces Conference.
40. Bazargan V., and Stoeber, B. Effect of substrate conductivity on the evaporation of small sessile droplets. *Physical Rev. E*, **94**, 033103 (2016).
41. Goel, P. et al. Effect of thermal conductivity on enhanced evaporation of water droplets from heated graphene–pdms composite surfaces. *Langmuir* **35**, (2019).
42. Dong, L., Zhang, Y., Liu, W., Yang, L. & Chen, J. A simple dielectric barrier discharge device for generating slot homogeneous plasma in atmospheric pressure air. *Appl. Phys. Lett.* **94**, 091502 (2009).
43. Bruggeman, P. et al. Dc excited glow discharges in atmospheric pressure air in pin-to-water electrode systems. *J. Phys. D: Appl. Phys.* **41**, 215201 (2008).
44. Vanraes, P., Nikiforov, A., Bogaerts, A. & Leys, C. Study of an AC dielectric barrier single micro-discharge filament over a water film. *Sci. Rep.* **8**, 10919 (2018).
45. Lu, X. and Laroussi, M. Ignition phase and steady-state structures of a non-thermal air plasma. *J. Phys. D: Appl. Phys.* **36**, 661–665 (2003).
46. Hou, S.-Y. & Chu, H.-Y. Saffman-taylor–like instability in a narrow gap induced by dielectric barrier discharge. *Phys. Rev. E* **92**, 013101 (2015).
47. Chu, H.-Y. & Lee, H.-K. Evolution of the plasma bubble in a narrow gap. *Phys. Rev. Lett.* **107**, 225001 (2011).
48. Thoroddsen, S. T. & Sakakibara, J. Evolution of the fingering pattern of an impacting drop. *Phys. Fluids* **10**, 1359–1374 (1998).
49. Sankaran, A. et al. Drop impact onto polarized dielectric surface for controlled coating. *Phys. Fluids* **33**, 062101 (2021).
50. Jae Hun, Kim. et al. Electrowetting-on-dielectric characteristics of ZnO nanorods. *Scientific Rep.* **10**, 14194 (2020).
51. Quetzeri-Santiago, M. A., Castrejón-Pita, J. R., and Castrejón-Pita, A. A. Scientific reports controlling droplet splashing and bouncing by dielectrowetting. *Scientific Rep.* **11**, 21410 (2021).
52. Liu, Y. & Hu, H. An experimental investigation on the unsteady heat transfer process over an ice accreting airfoil surface. *Int. J. Heat. Mass Transf.* **122**, 707–718 (2018).
53. Durscher, R., Stanfield, S. & Roy, S. Characterization and manipulation of the "saturation" effect by changing the surface temperature of a dielectric barrier discharge actuator. *Appl. Phys. Lett.* **101**, 252902 (2012).
54. Durscher, R. & Roy, S. Aerogel and ferroelectric dielectric materials for plasma actuators. *J. Phys. D: Appl. Phys.* **45**, 012001 (2011).

55. Ahumada Lazo, J. & Chen, R.-H. Self-similar behavior of successive coulombic fissions of evaporating charged water droplets. *Int. J. Heat. Mass Transf.* **219**, 124879 (2024).
56. Ahumada Lazo, J. & Chen, R.-H. Dynamic behavior of coulombic fissions and shell morphology of evaporating nanofluid droplets. *Int. J. Heat. Mass Transf.* **239**, 126519 (2025).
57. Ahumada Lazo, J. and Liu, Y. Dataset for paper: Droplet impact on plasma surfaces: An interplay of the four states of matter. https://doi.org/10.6084/m9.figshare.c.8036074.v1 (2025).
58. Jidenko, N., Bourgeois, E. & Borra, J.-P. Temperature profiles in filamentary dielectric barrier discharges at atmospheric pressure. *J. Phys. D: Appl. Phys.* **43**, 295203 (2010).

Acknowledgements

This material is based upon work supported by the U.S. Department of Energy, Office of Science, Office of Fusion Energy Sciences under award number DE-SC0024663.

Author contributions

Conceptualization, J.A.L. and Y.L. (equal); methodology, J.A.L. and Y.L. (equal); validation, Y.L.; formal analysis, J.A.L.; investigation, J.A.L.; resources, Y.L.; data curation, J.A.L. and Y.L.; writing—original draft preparation, J.A.L.; writing—review and editing, J.A.L. and Y.L. (equal); visualization, J.A.L.; supervision, Y.L.; project administration, Y.L.; funding acquisition, Y.L.

Competing interests

The authors declare no competing interests.

Additional information

Supplementary information The online version contains supplementary material available at https://doi.org/10.1038/s41467-025-64991-x.

Correspondence and requests for materials should be addressed to Yang Liu.

Peer review information *Nature Communications* thanks Miguel Quetzeri-Santiago, Patrick Vanraes and the other, anonymous, reviewer(s) for their contribution to the peer review of this work. A peer review file is available.